APPLIED SCIENCES AND ENGINEERING

Multimodal x-ray and electron microscopy of the Allende meteorite

Yuan Hung Lo[1,2], Chen-Ting Liao[3], Jihan Zhou[1], Arjun Rana[1], Charles S. Bevis[3], Guan Gui[3], Bjoern Enders[4], Kevin M. Cannon[5], Young-Sang Yu[4], Richard Celestre[4], Kasra Nowrouzi[4], David Shapiro[4], Henry Kapteyn[3], Roger Falcone[4], Chris Bennett[5], Margaret Murnane[3], Jianwei Miao[1]*

Multimodal microscopy that combines complementary nanoscale imaging techniques is critical for extracting comprehensive chemical, structural, and functional information, particularly for heterogeneous samples. X-ray microscopy can achieve high-resolution imaging of bulk materials with chemical, magnetic, electronic, and bond orientation contrast, while electron microscopy provides atomic-scale spatial resolution with quantitative elemental composition. Here, we combine x-ray ptychography and scanning transmission x-ray spectromicroscopy with three-dimensional energy-dispersive spectroscopy and electron tomography to perform structural and chemical mapping of an Allende meteorite particle with 15-nm spatial resolution. We use textural and quantitative elemental information to infer the mineral composition and discuss potential processes that occurred before or after accretion. We anticipate that correlative x-ray and electron microscopy overcome the limitations of individual imaging modalities and open up a route to future multiscale nondestructive microscopies of complex functional materials and biological systems.

INTRODUCTION

X-ray and electron microscopies visualize structure and function in organic and inorganic systems over spatial scales that range from tens of micrometers all the way down to the atomic scale. Recent advances in x-ray ptychography (*1*–*4*), which is a powerful coherent diffractive imaging (CDI) method (*5*), have extended soft x-ray imaging toward 5-nm spatial resolution (*6*, *7*). Ptychographic x-ray CDI has also demonstrated the ability to image extended integrated circuits (*8*, *9*) and biological structures (*10*–*14*) in two dimensions (2D) and three dimensions (3D), with sub–20-nm spatial resolution. Scanning transmission x-ray microscopy (STXM) with x-ray absorption spectroscopy (XAS) can map bulk specimens with 20-nm resolution; when performed in the soft x-ray regime, STXM can simultaneously extract chemical-specific maps of carbon, nitrogen, oxygen, and transition metals such as iron, manganese, and nickel (*15*) for materials and biochemically relevant samples. Exciting developments in electron microscopy, such as the introduction of cryogenic preservation of biological specimens at near-native conditions in thin amorphous ice films, as well as the introduction of aberration-corrected electron microscopes, have ushered in a new era of cryo–electron microscopy (*16*, *17*) and atomic electron tomography (*18*–*21*), thus enabling unprecedented imaging of materials and the associated structure-function relationships at a fundamental level.

Despite all the advancements, to date, no single imaging technique can provide a full comprehensive map of a sample—the limitations of each method dictate specific sample requirements, sizes, and the type of information that can be extracted. For instance, while electron microscopy offers unmatched atomic resolution, so far this method is only applicable to very thin samples owing to multiple scattering effects (*16*, *18*). In contrast, because of the high penetration ability of short wavelengths, x-ray microscopy can probe samples that are tens to hundreds of micrometers thick and, in addition, has substantially less stringent sample requirements than electron microscopy (*1*, *22*). However, the spatial resolution of 3D x-ray microscopy is currently below its theoretical limit due to technical challenges in achieving high coherent x-ray flux at synchrotron radiation facilities. Therefore, correlated electron and x-ray microscopies that take advantage of different contrast mechanisms can provide more comprehensive maps of a sample to solve challenging scientific problems.

Multimodal imaging has been implemented very successfully by the light microscopy (*23*, *24*) and medical imaging communities (*25*–*27*). In the case of x-ray and electron microscopies, multimodal imaging offers complementary advantages: high spatial resolution across multiple length scales, with ensemble elemental abundances and local atomic and chemical information. Combining these methods also offers potential strategies for alleviating sample radiation damage—x-rays have a higher sample damage threshold than electrons in inelastic scattering experiments, while electrons are more dose efficient than x-rays in elastic scattering experiments (*28*). Correlative imaging can also provide multifaceted experimental maps to guide computational modeling, thereby promoting rapid discovery and deployment of new materials to tackle scientific questions that would otherwise be too difficult to address (*29*). These challenges strongly motivate a new paradigm shift toward multimodal imaging that combines advanced x-ray and electron microscopies for studying the same specimen and take advantage of recent advances in sample preparation, imaging instrumentation, and synchrotron coherent radiation flux.

In this work, we investigate an Allende meteorite grain using x-ray ptychography and STXM in 2D, combined with energy-dispersive spectroscopy (EDS) and high-angle annular dark-field (HAADF) imaging in 3D. The Allende meteorite is a CV3 carbonaceous chondrite that was an observed fall in Mexico on 8 February 1969. Allende was well studied at the time because of laboratory facilities being prepared to receive lunar samples from the Apollo program. Allende consists of larger chondrules and calcium-aluminum–rich inclusions set in a fine-grained matrix of

[1]Department of Physics and Astronomy and California NanoSystems Institute, University of California, Los Angeles, CA 90095, USA. [2]Department of Bioengineering, University of California, Los Angeles, CA 90095, USA. [3]JILA and Department of Physics, University of Colorado and National Institute of Standards and Technology (NIST), Boulder, CO 80309, USA. [4]Advanced Light Source, Lawrence Berkeley National Laboratory, Berkeley, CA 94720, USA. [5]Department of Physics, University of Central Florida, Orlando, FL 32816, USA.
*Corresponding author. Email: miao@physics.ucla.edu

micrometer- to submicrometer-sized silicates, oxides, sulfides, and metals. The highly heterogeneous phase assemblage and various nanoscale petrographical characteristics are ideal for demonstrating the advantages of multimodal x-ray and electron microscopy techniques. As tomography is rapidly being adopted by the planetary science community, previous works have demonstrated 3D microscopy on Allende (*30*, *31*). In this study, we significantly enhance the spatial resolution achieved thus far (*32*) to infer the mineral composition and discuss potential processes that occurred before or after accretion. Our imaging results reveal many small internal textures and channels that strongly suggest shock veins and melt aggregates, while our spectroscopic measurements constrain the classifications of major meteoric components to silicates, sulfides, and oxides. This multidimensional study of the Allende meteorite provides possible hints into the origins and transport of refractory phases within the early solar nebula and highlights the potential of combined x-ray and electron imaging for studying heterogeneous materials.

METHODS

Sample preparation

Unsorted Allende meteorite fragments were placed in an agate mortar and immersed in ethanol and then gently pounded by an agate pestle into small grains of submicrometer thickness so that both soft x-rays and electrons can penetrate the sample. The resulting ethanol suspension was sonicated for 2 min for further dispersion. The supernatant solution was dropped using a pipette onto a carbon film on 200 mesh copper transmission electron microscopy (TEM) grids and air-dried on the grids for 24 hours before data acquisition.

STXM and ptychography data acquisition

STXM and x-ray ptychography data were recorded at beamline 7.0.1 in the Advanced Light Source (ALS) (*6*, *7*)—the Coherent Scattering and Microscopy (COSMIC) beamline—at the Lawrence Berkeley National Laboratory (LBNL). COSMIC provides monochromatic soft x-rays with energies ranging from 250 to 2500 eV, spanning the carbon and sulfur K-edges, and is optimized for spectromicroscopy of elements commonly found in mineral samples, including Fe, Ni, Mg, and Al. X-rays were focused using a Fresnel zone plate with a 45-nm outer zone width to give a total coherent flux of approximately 10^9 photons/s at the sample position. The sample substrate TEM grid was mounted onto a standard FEI CompuStage sample manipulator derived from an FEI CM200 series TEM and secured with a Hummingbird 3-mm half-grid tip. The use of a TEM-compatible sample holder was a crucial enabling technology that permitted seamless sample transfer between the x-ray and electron microscopes. Other commercially available TEM sample holders designed for tomography, cryo-tomography, and in situ experiments can also fit into the chamber environment. Once mounted, the sample chamber was pumped down to 1×10^{-6} torr. Diffraction data were recorded with a fast charge-coupled device camera developed by LBNL with the following specifications: 50 frames/s, 15-bit dynamic range with a 12-bit analog-to-digital converter, and 1 megapixel. Images were acquired without a beamstop.

STXM data were recorded with 10-ms dwell time using an 80 × 80 square scan grid that proceeded with 40-nm steps to cover a 3.2-μm by 3.2-μm field of view. XAS data can be collected using either point spectra at a single location, a line scan along a direction, or an image stack over a sequence of photon energies. We first performed a line energy scan to determine the correct absorption edge for the elements and then collected image stacks with energies varying across the absorption edge. Complete STXM-XAS image stacks using the above parameters were recorded at the Fe L_3-edge (707 eV), Ni $L_{2/3}$-edge (865/848 eV), Mg K-edge (1302 eV), and Al K-edge (1551 eV). Energy scan steps increased with 1-eV steps from 15 eV below the edge, then changed to 0.25-eV steps within ±5 eV of absorption resonance, followed by 1-eV steps to 15 eV above the edge. STXM energy stacks of each element took 30 to 60 min to record.

Ptychography data were recorded using double-exposure mode with 15/150-ms dwell times to enhance dynamic range and scanned in an 80 × 80 square grid with 35-nm steps to cover a 2.8-μm × 2.8-μm field of view. The resulting pixel size was 8 nm/pixel. Each ptychography image comprised 6400 diffraction patterns of 128 × 128 pixels. The total dose (D_p) deposited on the meteorite grain was estimated as $D_p = \left(\frac{P_1}{A}\right)\left(\frac{\mu}{\rho}\right)E$, where the fluence $\left(\frac{P_1}{A}\right)$ for 100-ms exposure is 6.46×10^{10} photons/μm^2, μ is the linear absorption coefficient, ρ is the average density of minerals, and μ/ρ was estimated to be 10 cm^2 g^{-1} with the average photon energy (E) at 1100 eV. The dose per projection was estimated to be 1.1×10^7 gray, which was within the tolerable dose for imaging at the resolution presented in this work (*33*). To compare absorption contrast differences for each element, ptychography images at both 5 eV below and directly on resonance were collected at the Fe L_3-edge, Ni $L_{2/3}$-edge, Mg K-edge, and Al K-edge. Phase retrieval of complex images was initially performed at COSMIC using the distributed graphics processing unit (GPU)–based ptychographic solver SHARP (*34*). To further improve reconstruction quality and to remove artifacts due to the rectilinear scanning grid, final ptychographic images presented in our results were refined using a parallel ptychography reconstruction algorithm (*35*, *36*), with an update condition derived from the hybrid projection-reflection algorithm (*37*–*40*). Each reconstruction ran for 5000 iterations, where the probe was updated continuously after the fifth iteration.

HAADF and EDS data acquisition

Electron tomography data were collected at the National Center for Electron Microscopy. For TEM experiments, a Titan 60-300 equipped with a HAADF detector (Gatan, Pleasanton, CA) and four windowless silicon drift EDS detectors (FEI Super-X) were used with a solid angle of 0.7 srad. The microscope operated in scanning transmission electron microscopy (STEM) mode at 200 kV with an electron beam current of ~550 pA for STEM-EDS maps and ~40 pA for HAADF-STEM imaging. A typical total dose for the complete tomography series was ~1300 e$^-$/Å^2, and a typical total dose for an EDS map was ~1100 e$^-$/Å^2. EDS data were collected as a tilt series of scanned spectrum images, which measured emitted x-rays from regions probed by the electron beam. The images were drift-corrected over ~120 s, assuming a time-dependent linear drift model at different tilt angles.

HAADF-STEM scans and probes local structural information by collecting electrons scattered onto the HAADF detector. All tilt series of projection images were typically acquired between −64° and 72°, with a linear tilt step of 2°. The tilt range was limited by the shadowing of the sample holder (Hummingbird, Lacey, WA). HAADF-STEM images were acquired with a convergence semi-angle of 10 mrad at a detector inner semi-angle of 63 mrad and outer semi-angle of 305 mrad. Image size was 1024 × 1024 pixels with a pixel size of 4.67 nm. Each projection image was binned by 3 to have a pixel size of 14.01 nm. We carefully checked the integrity of the samples before and after taking tomographic tilt series using zero-degree projections and before and after EDS mapping. We observed no visible sample damage.

HAADF, EDS, and XAS data analysis

Tomography reconstruction was performed using the GENeralized Fourier Iterative REconstruction (GENFIRE) algorithm (*41*). Before reconstruction, elemental tilt series of C, O, Mg, Al, Si, S, Cr, Fe, and Ni were extracted from the EDS spectra using Python's HyperSpy package (*42*) for multidimensional data analysis. HAADF and EDS projections were aligned to a common tilt axis using the center of mass and common line methods (*19*). The background was subtracted from each projection by removing the average value in an empty region of the sample, and the process was optimized by minimizing the differences between common lines. Next, projections were normalized to have the same total sum, as the integrated 3D density of the sample should be constant. Each GENFIRE reconstruction ran for 100 iterations, using an oversampling ratio of 2 and a 0.7-pixel interpolation distance, and with positivity and support constraints enforced.

Elemental abundances in the meteorite grain were estimated from the zero-degree EDS image using HyperSpy. The spectral data were a 3D array, where x and y axes corresponded to probe positions and the z axis corresponded to the energy of detected x-rays. Non-negative matrix factorization was used to decompose data dimensionality and segment regions based on spectral similarities. Net x-ray intensities were obtained in HyperSpy by sampling and integrating the background-subtracted spectrum peaks at the elements of interest. To obtain quantitative elemental compositions at subregions of the grain, mass fractions were quantified using the Cliff-Lorimer equation (*43*), $\frac{I_1}{I_2} = k_{12}^* \frac{C_1}{C_2}$, where I_i and C_i are the integrated peak intensities and mass fractions of the ith element, respectively, and k_{12}^* is the thickness-corrected Cliff-Lorimer sensitivity factor ("k-factor") between elements 1 and 2. For more than two species, the formula becomes $\Sigma_{i=1,2,3,\ \ldots} C_i = 1$. The default k-factors were provided by EDS system manufacturer Bruker software and account for detector sensitivity to different elements' dispersed x-rays. Thickness correction was applied to the vendor-supplied k-factors to obtain k_{12}^* (*44*), which accounts for non-negligible absorption and fluorescence effects in the thick sample, and was calculated using the average grain thicknesses estimated from EDS tomography results.

Local chemical information in the meteorite was provided by STXM-XAS analysis using the MANTiS software (*45*). A series of STXM transmission images recorded at different incident x-ray energies spanning different atomic resonances were first converted to optical densities using fully transmitting regions in the specimen. Hot pixels were replaced by the average value in the surrounding pixels, and the background was subtracted. The image stack was then aligned iteratively using the center of mass and common line alignment methods. Next, spectra in the 3D image stack were decomposed using principal components analysis (PCA) and k-means clustering to group spectra with similar spectral signatures. Last, singular value decomposition without reference spectra was used to produce chemical maps and their corresponding absorption spectra.

Ptychography data analysis with SQUARREL

To derive quantitative elemental information from the complex (amplitude and phase) ptychography images, here, we introduced a new semiquantitative analysis method in x-ray ptychography, named Scattering QUotient Analysis to REtrieve the Ratio of ELements (SQUARREL). In this method, the complex ptychographic images are used to calculate the scattering quotient map (f_q) (*46*–*48*), which is defined as $f_q \equiv \frac{\ln(|T(x,y;E)|)}{\phi(x,y;E)} = \frac{\Sigma_i N_i(x,y;E)\beta_i(E)}{\Sigma_i N_i(x,y;E)\delta_i(E)} = \frac{\Sigma_i N_i(x,y;E) f_{Ii}(E)}{\Sigma_i N_i(x,y;E) f_{Ri(E)}}$. $|T(x, y; E)|$ and $\phi(x, y; E)$ are the transmission magnitude image ($0 \leq |T| \leq 1$) and the phase retardation image ($\phi \leq 0$) of the complex transmission function, or $T(x, y; E) = |T(x, y; E)| \exp[i\phi(x, y; E)]$, that was acquired by ptychography at an x-ray photon energy (E). N_i is the atomic number density of the ith element in the sample. β and δ are the imaginary and real part of the complex refractive index (n) decrement, respectively. f_{Ii} and f_{Ri} are the imaginary and real part of complex atomic scattering factors, respectively, where $n = 1 - \delta + i\beta \propto (1 - f_{Ri} + if_{Ii})$. Note that the complex atomic scattering factors are averaged values along the projection through the sample and $f_q \geq 0$.

The scattering quotient is, in principle, independent of sample thickness variation since the thickness has been canceled out in the quotient (*48*, *49*). As a result, the scattering quotient is especially suitable for studying inhomogeneous specimens where conventional analysis methods cannot distinguish thickness variations from changes in refractive indices of different compositions, since both thickness and composition variations contribute to changes in light absorption and phase retardation. The scattering quotient map images have been used as a previously unidentified contrast mechanism in materials (*50*–*52*) and as an image segmentation and classification method for biological samples (*48*, *49*). The key idea to SQUARREL is to convert a scattering quotient map to a two-element ratio map, $R_a = R_a(f_q; E)$, given a fixed amount of a third element as a priori knowledge. The two-element ratio conversion function (R_a) is derived by a direct comparison to a theoretical calculation, which is based on the tabulated complex refractive indices from The Center for X-Ray Optics (CXRO) or National Institute of Standards and Technology (NIST) Standard Reference Database (*53*) of the mixture in atomic %.

For example, given a priori knowledge of a possible compound or a mixture Z ($Z = X_pY_qV_r$) with X, Y, V elements and with p, q, r atoms, the conversion function can be calculated to provide a two-element ratio, e.g., a q-to-p ratio at a given r. The mixture's atomic number density reads $N_Z = N_{AV}(p\rho_X + q\rho_Y + r\rho_V)/(pMX + qMY + rMV)$, where N_{AV} is the Avogadro constant, $\rho_{X,\ Y,\ V}$ are the individual constituent's mass number density, and $M_{X,\ Y,\ V}$ are the individual constituent's atomic mass number. We can then get the individual constituent's atomic number density, $N_X = pN_Z$, $N_Y = qN_Z$, $N_V = rN_Z$, to finish the theoretical scattering quotient calculation of the mixture Z. After choosing an appropriate x-ray photon energy (E), i.e., a horizontal line out from fig. S15, the two-element conversion function, $R_a(E)$, behaves as a smooth and monotonic function, which correlates f_q and R_a. Therefore, we can convert scattering quotient maps into two-element ratio maps.

RESULTS

HAADF and EDS tomography

Figure 1 shows the schematics of the multimodal electron and x-ray spectral imaging setup, where HAADF and EDS tomography were performed on the same Allende meteorite grain deposited on a carbon-coated TEM grid and then later transported to the COSMIC beamline for x-ray imaging. Slices through the GENFIRE HAADF reconstruction of the grain showed various internal morphologies that revealed different phase assemblages (Fig. 2A and fig. S1). The reconstruction spatial resolution was estimated to be approximately 15 nm using the 10 to 90% knife edge method (fig. S13A). In the larger meteorite matrix, we observed long internal channels, 20 to 50 nm in diameter, that were suggestive of shock veins (Fig. 2A, green arrow). Adjacent to the matrix were two high-intensity spherical granules that are representative of melt pockets (Fig. 2A, red and teal arrows).

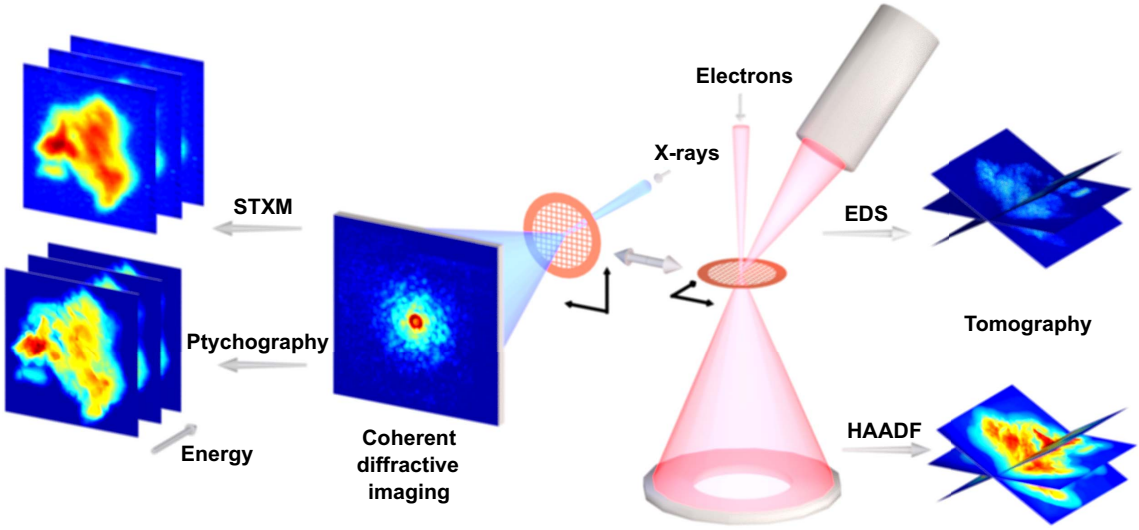

Fig. 1. Multimodal x-ray and electron nanoscopic spectral imaging scheme. Allende meteorite grains deposited on a TEM grid were transferred between a Titan 60-300 electron microscope and the COSMIC soft x-ray beamline for tomographic, ptychographic, and spectromicroscopic imaging. COSMIC's TEM-compatible sample holder enabled the same meteorite grain to be imaged using both imaging modalities to extract multidimensional datasets, providing chemical, structural, and functional insights with high spatial resolution.

Next, we determined the grain's elemental compositions using EDS tomography to understand the textural differences between various regions. EDS signal indicated the presence of C, O, Mg, Al, Si, S, Cr, Fe, and Ni in the grain (Fig. 2B and figs. S2 to S10 and S14). The superimposed EDS and HAADF GENFIRE reconstructions revealed three main mineral domains: (i) iron-magnesium silicate (Fig. 2B, purple and teal), (ii) aluminum-chromium iron oxide (Fig. 2B, yellow), and (iii) iron-nickel sulfide (Fig. 2B, red). Note that the gradual transition between Fe and Mg contents at different depths in the iron-magnesium silicate can be seen in 3D. To quantify elemental abundances, we applied the Cliff-Lorimer ratio method (*43*) on the integrated peak intensities to obtain the elements' relative concentrations (Methods; fig. S14). On average, the iron-magnesium silicate was 13% Fe, 18% Mg, 49% O, and 20% Si; the aluminum-chromium iron oxide was 25% Al, 29% C, 5% Cr, 4% Fe, and 37% O; and the iron-nickel sulfide was 28% Fe, 22% Ni, and 50% S. Note that the buildup of C contamination on the sample during data acquisition contributed to the high C composition in the analysis, which should normally be approximately 1%. The elevated C composition could also be attributed to the large variation in absorption as the sample tilts relative to the EDS detector, which could be especially pronounced for elements with large mass absorption coefficients such as C. As the sample was tilted to different angles, the heterogeneity in the sample might cause huge point-to-point variations in absorption, which could artificially elevate the apparent C abundance. On the basis of elemental quantification, the large mass of iron-magnesium silicate is likely olivine, pyroxene, or serpentines, all of which are high-temperature primitive nebular condensates commonly found in carbonaceous chondrites and interplanetary dust particles. The oxides and metal sulfides adjacent to the host rock typically condense over a similar range of temperatures. Together with the silicates, the proximity of these three mineral phases confirms the high-temperature nebular environment of the grain's accreted components (*54*).

Ptychography and STXM-XAS

To complement the electron microscopy results, we used differential x-ray absorption contrast to study elemental locations and abundances in more detail. We collected 2D ptychography images of the grain on and below the core level absorption resonance energies for Al, Fe, Mg, and Ni, the four major elements in the grain (fig. S11). The spatial resolution was estimated to be approximately 20 nm using the 10 to 90% knife edge method (fig. S13B). By dividing the on-edge and pre-edge absorption images of each element, we can pinpoint the locations of each element with high contrast and spatial resolution (Fig. 3, A to D). In general, the spatial distributions of the four elements agreed well with those observed in the EDS data. However, upon closer inspection, we observed regions with higher Fe concentration in the silicate that coincided with the Al melt pockets and veins (Fig. 3, A and B, red arrows). While the Al melts were visible in EDS tomography, the colocation of Fe in the same melts was difficult to detect in EDS. This is because the overall Fe contrast in the melts was lowered by being embedded in the large iron silicate. Although EDS did not have sufficient contrast or resolution to discern the presence of Fe in the vein, x-ray absorption at the Fe L-edge was able to provide enough sensitivity to detect these fine chemical differences. The Mg absorption difference image did not show the presence of Mg in the same melts (Fig. 3C, red arrows), as evidenced by the large gaps where the melts should be, which suggests that Mg might not have melted under high temperature.

In addition to providing sensitive chemical localization in the grain, complex ptychography images can also be used to quantitatively estimate elemental compositions by our newly developed SQUARREL method. As a proof-of-principle demonstration, we quantified the Ni and Fe content in the iron-nickel sulfide region, consistent with pentlandite [$(Fe,Ni)_9S_8$] (*55*). The empirical compound formula of the sulfide is $Fe_pNi_qS_{0.89}$, where $p + q = 1$. We first calculated scattering quotients of the logarithmic transmission magnitude and the phase retardation images from the ptychographic images as shown in fig. S11. To apply SQUARREL, we then calculated the theoretical complex refractive indices of the iron-nickel sulfide.

The calculated sum ($\Sigma_i N_i \delta_i$) of the atomic number density (N_i) and real decrement part (δ_i) of the complex refractive indices of $Fe_pNi_qS_{0.89}$ are shown in fig. S15A. Similarly, the calculated sum ($\Sigma_i N_i \beta_i$) of the atomic number density and imaginary decrement part (β_i) of the

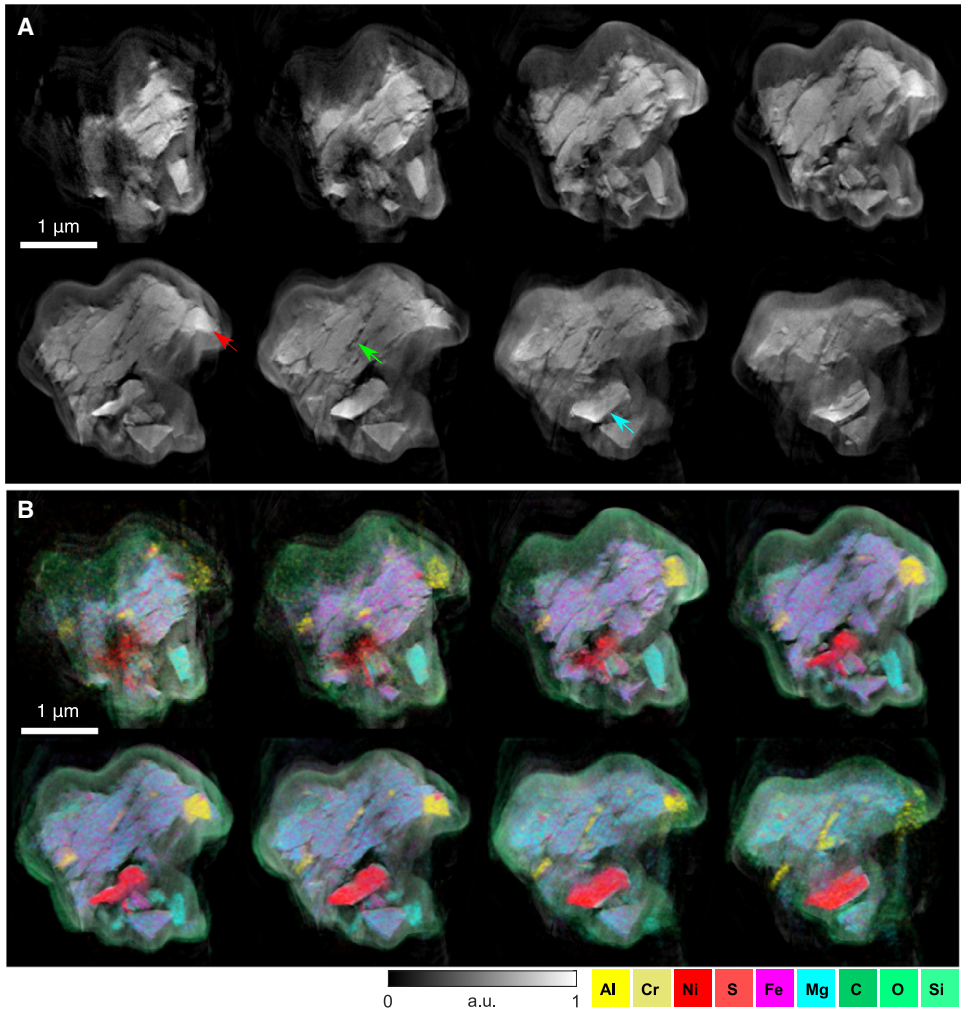

Fig. 2. HAADF and EDS GENFIRE tomography reconstructions. Representative 14-nm-thick layers in the reconstructed 3D HAADF (**A**) and EDS (**B**) volumes of the Allende meteorite grain. The red arrow points to melt pockets, and the green arrow points to shock veins that were embedded, which suggest that the sample had at some point experienced impact-induced heating, cracking, and melting. The traces of aluminum and chromium in the veins that are visible in the EDS reconstructions reveal that the veins were filled with metallic recrystallization. a.u., arbitrary units.

complex refractive indices are shown in fig. S15B. Both sums are normalized to N_{AV} for convenience. The calculated scattering quotient f_q (fig. S15C) is simply the quotient of fig. S15 (A and B). We can then convert a scattering quotient to a two-element, *q*-to-*p*, ratio, which is the key of SQUARREL. In principle, any horizontal line out from fig. S15C can be used as a conversion function. However, practically speaking, a monotonic and smooth function far from resonance, i.e., elemental absorption edges, works much better since it is less prone to noise or other uncertainties. As such, one should avoid choosing an x-ray spectral range adjacent to an elemental absorption energy; i.e., no resonant absorption is needed in the SQUARREL method. Furthermore, choosing a range with a monotonic function assures that the conversion is unique.

Figure 3 shows two scattering quotient maps for Mg pre-edge (Fig. 3E) and Al pre-edge (Fig. 3F) images. This region of interest is shown in Fig. 3B (dashed red rectangle). The maps present different and novel image contrast compared to conventional XAS images or phase-contrast images. Complete scattering quotient maps derived from all ptychographic images (fig. S11) are shown in fig. S16. Figure 3 shows the Fe-to-Ni ratio maps derived from Mg pre-edge (Fig. 3G) and Al pre-edge (Fig. 3H) images, where 100% implies a pure nickel sulfide mixture without iron. In general, the converted ratio maps from both pre-edges agree well with each other, despite small differences that could be attributed to uncertainties that will be discussed later. On the basis of the Ni-Fe ratio maps extracted from SQUARREL, the Ni:Fe in the region of interest of our sample is around 1:1 and is consistent with the nominal Ni:Fe in pentlandite, which further supports our assumption of the iron-nickel sulfide as pentlandite.

Besides ptychography, XAS can act as a fingerprint to understand the meteorite's phase assemblages and redox states. We collected STXM-XAS images across the Fe L_3-edge, Ni $L_{2/3}$-edge, Mg K-edge, and Al K-edge and analyzed them for unique spectral characteristics (fig. S12). PCA generated representative absorption spectra of the four major elements in the grain: Al, Fe, Mg, and Ni (Fig. 3, I to L). The Al K-edge spectrum agreed well with the spectrum of Al_2O_3 published elsewhere (*56*). The Ni $L_{2/3}$-edge spectrum is similar to that of synthetic nickel sulfide and pure nickel (*57*, *58*), while the overall Mg K-edge spectral signature was consistent with those of magnesium silicates (*59*).

PCA returned two unique Fe spectra (Fig. 3J), whose spectral signatures closely match published reference spectra (*60*) of iron silicate

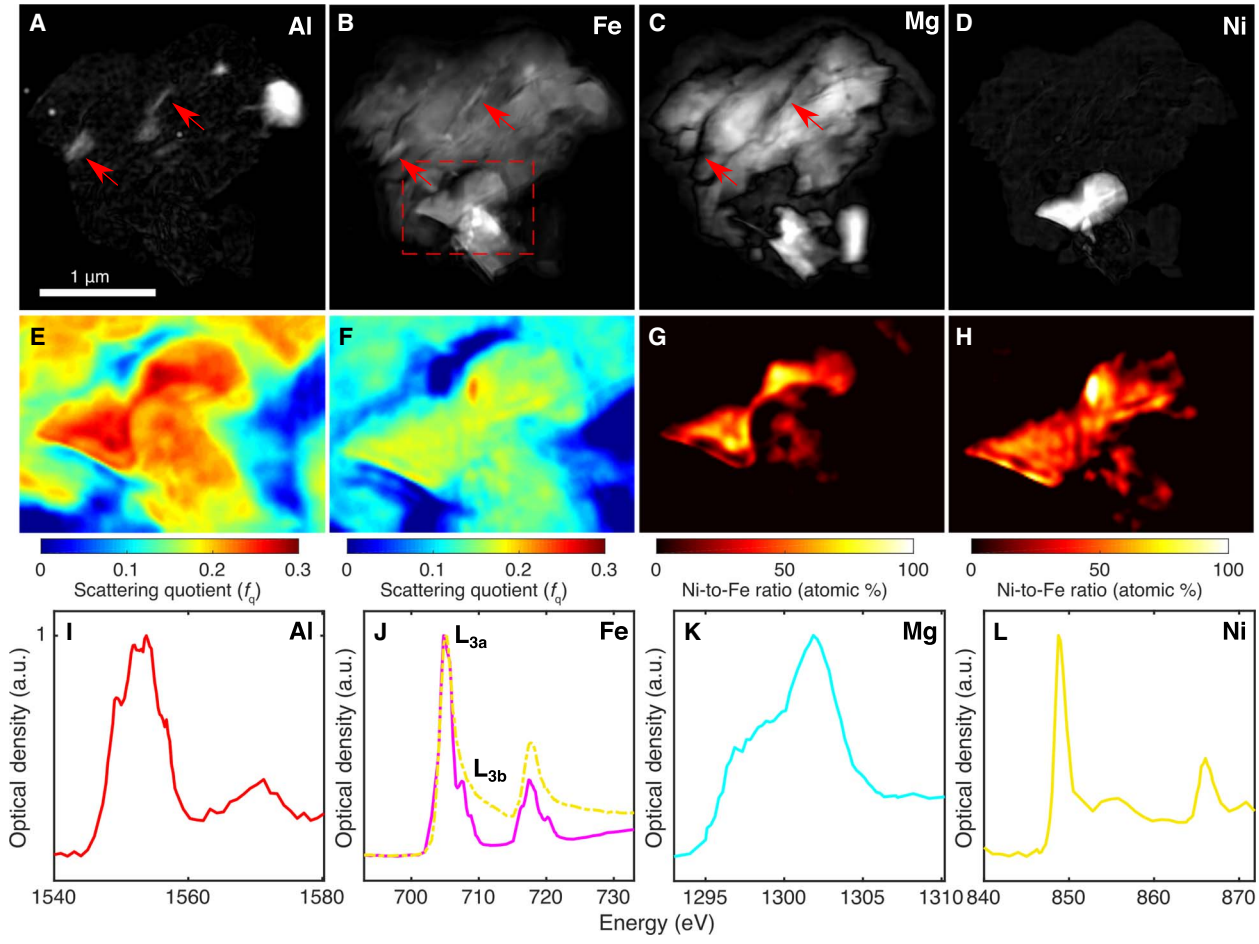

Fig. 3. X-ray ptychography and STXM absorption spectromicroscopy. (**A** to **D**) Localization of major elements in the meteorite revealed by dividing pre-edge and on-edge ptychography images at the absorption edges for Al, Fe, Mg, and Ni. The absorption quotient maps, displayed in logarithmic scale, show the presence of Fe in the shock veins of the silicate that is barely observable in EDS images (red arrows). (**E** and **F**) Scattering quotient (f_q) maps derived from ptychographic Mg pre-edge and Al pre-edge images, respectively. This region of interest is a zoomed-in view from the dashed red rectangle shown in (B). (**G** and **H**) Ni-Fe ratio maps from Mg pre-edge and Al pre-edge scattering quotient maps, respectively. These ratio maps are converted using the SQUARREL method, given a fixed amount of sulfur. The color bar indicates the Ni-Fe ratio and 100% implies a pure nickel sulfide region. (**I** to **L**) Absorption spectra generated from STXM energy scans across the four absorption edges, revealing unique spectral fingerprints for each respective element and also showing pronounced spectral differences in the different iron-containing regions. Relative peak intensities between Fe L_{3a} and L_{3b} also reveal the presence of predominant Fe^{2+} species. Colors of the solid lines match colors of mineral regions in Fig. 2B.

(Fig. 3J, solid purple line) and iron sulfide (Fig. 3J, dashed yellow line). Moreover, the regions represented by the two spectra precisely match the iron-magnesium silicate and iron-nickel sulfide previously identified in EDS and ptychography, further substantiating the presence of different Fe chemical states in the grain. In the case of iron silicate, the relative Fe L_{3a} and L_{3b} peaks are anticorrelated and dependent on the Fe redox state, where the L_{3a} peak increases linearly relative to the L_{3b} peak as $Fe^{3+}/\Sigma Fe$ ratios decrease (*61*). Since L_{3b} has a higher peak intensity than L_{3a}, we concluded that the Fe in the iron silicate was mostly in its reduced Fe^{2+} form. This ability to distinguish different mineral polymorphs is a strong advantage of the XAS over EDS and highlights the complementary nature of x-ray and electron microscopy.

DISCUSSION

The combination of x-ray and electron microscopy for studying the Allende meteorite yields complementary information about the structural and chemical states of this heterogeneous sample. In combination, this information can help identify the possible mineral phases present in the meteoric grain with nanometer spatial resolution. Figure 4 shows the ternary phase diagrams derived from the Cliff-Lorimer ratios calculated using the EDS data. They plot the compositions of major elements in iron-nickel sulfide, iron-magnesium silicate, and aluminum-chromium iron oxide regions of the grain. Some other mineral types with similar elemental makeup are included for reference.

Comparisons between these compositions suggest that the sulfide is likely a pentlandite $[(Fe,Ni)_9S_8]$ and that the oxide belongs to the chromite-hercynite spinel series $[Fe(Cr,Al)_2O_4]$. XAS results for Al, Mg, and Ni all show spectral fingerprints that are consistent with their respective mineral phases as found in the literature. As for the silicate, analysis of Fe x-ray absorption spectra shows the Fe with a predominantly +2 oxidation state, which narrows down possible mineral candidates to ferrosilite $[(Fe^{2+},Mg)_2Si_2O_6]$, wadsleyite $[(Mg,Fe^{2+})_2SiO_4]$, or more likely olivine $[(Mg,Fe^{2+})_2SiO_4]$ (*62*, *63*), and excludes candidates such as majorite $[Mg_3(Fe^{3+},Al,Si)_2(SiO_4)_3]$. Together, analyses from both x-ray and electron microscopy data helped narrow down the identities

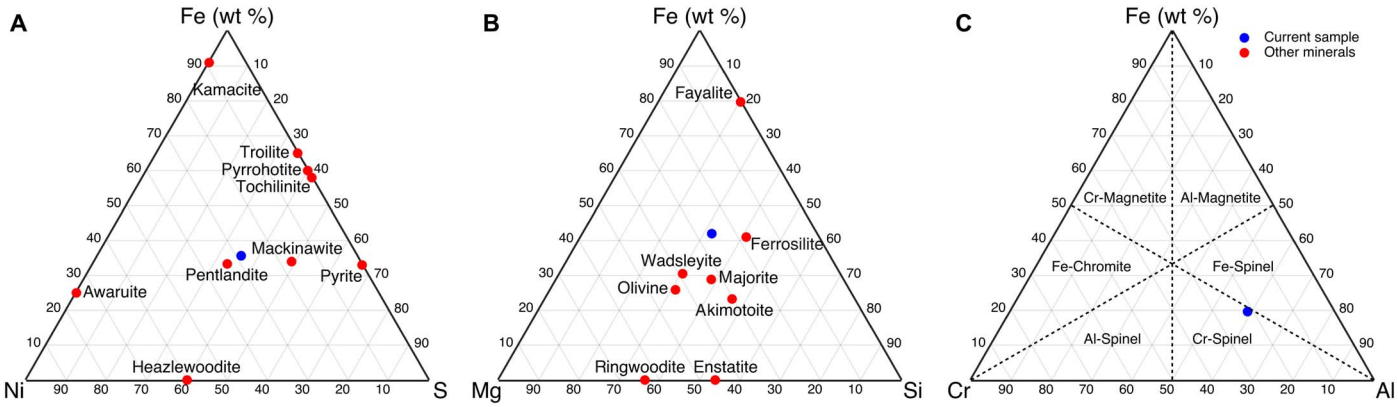

Fig. 4. Possible grain composition based on EDS quantification of elemental abundances. Ternary plots of major elements as quantified by the Cliff-Lorimer method for three different mineral types in the meteoric grain. Quantitative compositional information narrows down the possible mineral types and suggests that the sulfide is similar to pentlandite (**A**), the silicate is similar to ferrosilite (**B**), and the oxide is a chromium spinel or chromite (**C**). wt %, weight %.

of the various phase assemblages and provided a detailed nanoscopic petrographical picture of the meteorite grain.

Moreover, using the SQUARREL method from x-ray images, we quantified the Ni and Fe composition in the iron-nickel sulfide region and reaffirmed the identity of pentlandite that was predicted by EDS analysis. Theoretically, both Mg pre-edge and Al pre-edge scattering quotient maps should provide the same—or at least very similar—nickel-to-iron ratio maps. However, several possible sources of uncertainties and errors can affect the result's accuracy. The conversion functions based on Mg and Al pre-edge energies are offset by the same constant to account for systematic errors or uncertainties and to ensure that the ratio is within 0 to 100%. Given uncertainties in the x-ray energies used in our experiments, we also calculated the variation of the conversion function based on different x-ray photon energies, namely, shifted horizontal line outs from fig. S15C. When the x-ray energy varied ±5 eV around Mg pre-edge energy (E = 1295 eV), the resulting conversion function, $R_a = R_a(f_q; E)$, returned ~5% change in the q-to-p ratio. To test the robustness of this conversion, we also calculated the mixture with a slightly different amount of sulfur. When the amount of sulfur was varied from 0.85 to 0.95, the resulting q-to-p ratio changes ~10%.

To further test the robustness of SQUARREL, we also included a fourth element in the mixture so that the mixture now becomes $Fe_pNi_qS_{0.89}W_l$, where the fourth element "W" could be Al, Mg, Si, C, or O. The inclusion of these potential elements was based on our EDS analysis. From this calculation, we found that including additional elements did not have large effects (~5%) on the q-to-p ratio. Assuming uncorrelated sources of uncertainties or errors, we calculated the statistical variation based on the product of independent variables. This provides the SD of the uncertainty on the order of 12% (i.e., $\sqrt{5\%^2 + 10\%^2 + 5\%^2}$), accounting for the SQUARREL method's total uncertainty. Last, we note that the SQUARREL method relies on tabulated data from the CXRO database, which might introduce additional unaccounted uncertainties. According to (*64*, *65*), the estimated uncertainties of the current CXRO tabulation could be off by 3 to 10% at x-ray energies ranging from 500 to 1000 eV and could be off by as much as 20 to 30% near x-ray elemental absorption edges. Note that in the future, these sources of error can be reduced with additional calibration measurements.

Regardless of those uncertainties, SQUARREL analysis of ptychography data provides semiquantitative two-element ratio compositions with spatial specificity, and it confirms the elemental distributions observed in EDS. Extracting an accurate nickel-to-iron ratio is very important for identifying different mineral phases (*66*, *67*), and SQUARREL could serve as a general and complementary nondestructive analysis tool with EDS to quantify compositions in thickness-varying and heterogeneous samples. Last, we note that because we implemented correlative electron and x-ray imaging, the main scientific findings regarding the Allende meteorite do not rely on SQUARREL. Instead, the mineral phase identification is done using the well-established STEM EDS, with complementary information from STXM absorption spectromicroscopy. The SQUARREL method is presented here as a proof-of-concept demonstration to introduce a new complementary method that can be used for future nondestructive elemental composition identification, particularly of rare samples.

An extension of SQUARREL to include more elements without a priori knowledge of a third element is also possible and is worth exploring in future work. This extension could extend to a general multielement ratio quantification method for x-ray and even extreme ultraviolet ptychography (*38*–*40*). The combined usage of scattering quotient and quantitative phase images from ptychography created a new analysis method that can be used to derive semiquantitative composition information (*68*).

Besides identifying possible mineral types, HAADF tomography and x-ray ptychography provide high-resolution textural information to explain possible processes that affected the Allende parent body during and after accretion. In general, shock melting causes a series of changes in meteorites, starting with the generation of localized shock veins and pockets, followed by the transformation of minerals to high-pressure polymorphs and the formation of diaplectic glass, and then end with the recrystallization of highly deformed minerals (*69*, *70*). High-resolution views of the mineral's internal morphologies in Figs. 2B and 3B show the silicate filled with nanoscopic Fe, Al, and Cr veins, which provide strong evidence of melts resulting from impact shocks and heat-induced metamorphism (*71*, *72*). Moreover, the absence of Mg in the same veins shown in the ptychography difference maps (Fig. 3C) indicates no Mg in the veins or that no melting of Mg-bearing phases occurred.

In summary, the evidence gathered from the two imaging modalities agrees well with previous 2D studies of Allende (*73*, *74*) at a coarser resolution, but the nanoscale resolution provides the ability to study fine-grained matrix material in greater detail and the observed melt channels provide insight into processes that cannot be seen at larger scales. The

different phases identified are high-temperature refractory nebular condensates (*54*), some of which may have formed in the hotter inner parts of the solar nebula and were later transported out to the cooler carbonaceous chondrite region of the protoplanetary disk (*75*). In this particular sample studied, there are no obvious chondrules, and the assemblage represents the agglomeration of primitive fine-grained silicate dust in the nebula. Allende is classified as shock stage S1 or unshocked, but its parent body had to have experienced large-scale impact events during accretion and at a later time to dislodge meteorites. The nanoscale melt channels seen in this work may provide evidence of these impacts, and further study could constrain the pressures and timing (pre-accretion versus post-accretion) of the melting events.

In addition to the meteorite samples discussed in this work, many other interesting materials with heterogeneous compositions, domains, phases, and defects can benefit from this multimodal microscopy approach. Studies of complicated samples require both macroscopic and microscopic investigations to provide multidimensional morphological and chemical information.

Here, we also suggest a potential strategy for improving this multimodal approach. First, one could use x-ray ptychography to probe bulk samples that are tens of micrometers in size to understand aggregate chemical and structural properties with few-nanometer spatial resolution. Next, atomic electron tomography (*21*) can be used to probe select regions on the sample surface that are a few nanometers thick to create 3D atomic models of boundary morphologies. This atomic information can correlate with bulk x-ray observations to provide a comprehensive, multiple–length scale investigation into a single specimen. Unlike other nanocrystallographic approaches that may rely on the use of a focused ion beam to destructively section bulk specimens for STEM–electron energy-loss spectroscopy or electron diffraction, the nondestructive multimodal imaging paradigm proposed here is especially suitable for probing scarce extraterrestrial samples (e.g., from Stardust, Hyabusa, or OSIRIS-REx missions), which are extremely rare and should therefore not be destroyed after a single measurement.

In addition, correlative measurements of the same sample recorded with different modalities can be used synergistically to reduce overall data requirement. For instance, ptychography reconstructions are known to benefit from having accurate input probe or object initializations, which may be provided by HAADF-STEM. Accurate prior knowledge can help ptychography algorithm converge faster and may also reduce data redundancy necessary to achieve good results. In the future, similar strategies can be explored with other modalities to formulate a dose-efficient data acquisition scheme for 2D and 3D correlative imaging.

Other than methodology development, several improvements in x-ray microscopy will enhance the applicability of this multimodal method. Currently, synchrotron-based ptychography is still flux-limited, with each acquisition taking on the order of tens of minutes to hours. As such, ptychographic spectromicroscopy is still not practical for most experiments. Nonetheless, the upcoming ALS Upgrade (*76*) will offer at least 100 times brighter soft x-rays than what is currently available, which will markedly reduce data acquisition time and push toward new resolution limits. As for dealing with sample radiation damage, more x-ray microscopy beamlines are currently implementing cryogenic capabilities, which will allow radiation-sensitive samples to be probed repeatedly with minimum damage. Moreover, efforts to develop advanced inter-instrument sample transfer mechanisms as well as data collection and processing workflows are currently underway. In the future, a fully consolidated sample environment will allow seamless sample transfer between x-ray and electron microscopes for sequential imaging and will enable studies of delicate samples or samples in situ.

CONCLUSION

In this work, we demonstrated a new multimodal imaging approach by combining HAADF and EDS tomography with x-ray ptychography and STXM absorption spectromicroscopy to study a small subsection of the Allende CV3 carbonaceous chondrite meteorite. We also introduced a new semiquantitative ptychography analysis method, named SQUARREL, for determining elemental compositions in a mixed material. The synergistic relationship between electron and x-ray imaging and their complementary advantages are highlighted. The multidimensional data provided quantitative chemical and textural information on the diverse phase assemblage in the meteorite grain. Quantifying relative elemental abundances in the phase assemblage suggests the classifications of rock-forming silicates as pyroxenes or olivine, sulfide as pentlandite, and oxide as chromium spinel. This assemblage is consistent with previous studies of Allende that reveal a fine-grained matrix consisting of refractory nebular condensates. Morphological studies of the assemblage reveal nanoscopic metallic shock veins and pockets filled with Al, Fe, and Cr. The observation of shock veins suggests that the Allende parent body or accreted components experienced impact-induced melting at some stage. As this multimodal imaging approach continues to develop beyond this initial demonstration and toward intramodal integration, we expect it to be useful for probing complicated heterogeneous systems and gaining new insights across multiple length scales.

SUPPLEMENTARY MATERIALS

Supplementary material for this article is available at http://advances.sciencemag.org/cgi/content/full/5/9/eaax3009/DC1

Fig. S1. Experimental HAADF tilt series.
Fig. S2. Experimental aluminum channel EDS tilt series.
Fig. S3. Experimental iron channel EDS tilt series.
Fig. S4. Experimental magnesium channel EDS tilt series.
Fig. S5. Experimental nickel channel EDS tilt series.
Fig. S6. Experimental sulfur channel EDS tilt series.
Fig. S7. Experimental oxygen channel EDS tilt series.
Fig. S8. Experimental silicon channel EDS tilt series.
Fig. S9. Experimental chromium channel EDS tilt series.
Fig. S10. Experimental carbon channel EDS tilt series.
Fig. S11. Ptychography near Al, Fe, Mg, and Ni edges.
Fig. S12. STXM spectromicroscopy.
Fig. S13. Achieved spatial resolution for ptychography and HAADF microscopy.
Fig. S14. EDS spectral decomposition.
Fig. S15. Calculated conversion functions used in SQUARREL for iron-nickel sulfide.
Fig. S16. Scattering quotient maps providing a novel contrast.

REFERENCES AND NOTES

1. J. Miao, T. Ishikawa, I. K. Robinson, M. Murnane, Beyond crystallography: Diffractive imaging using coherent x-ray light sources. *Science* **348**, 530–535 (2015).
2. F. Pfeiffer, X-ray ptychography. *Nat. Photonics* **12**, 9–17 (2018).
3. R. Falcone, C. Jacobsen, J. Kirz, S. Marchesini, D. Shapiro, J. Spence, New directions in X-ray microscopy. *Contemp. Phys.* **52**, 293–318 (2011).
4. A. P. Hitchcock, Soft X-ray spectromicroscopy and ptychography. *J. Electron Spectrosc. Relat. Phenom.* **200**, 49–63 (2015).
5. J. Miao, P. Charalambous, J. Kirz, D. Sayre, Extending the methodology of X-ray crystallography to allow imaging of micrometre-sized non-crystalline specimens. *Nature* **400**, 342–344 (1999).
6. R. Celestre, K. Nowrouzi, D. A. Shapiro, P. Denes, J. M. Joseph, A. Schmid, H. A. Padmore, Nanosurveyor 2: A compact instrument for nano-tomography at the advanced light source. *J. Phys. Conf. Ser.* **849**, 012047 (2017).

7. D. A. Shapiro, R. Celestre, P. Denes, M. Farmand, J. Joseph, A. L. D. Kilcoyne, S. Marchesini, H. Padmore, S. V. Venkatakrishnan, T. Warwick, Y.-S. Yu, Ptychographic imaging of nano-materials at the advanced light source with the nanosurveyor instrument. *J. Phys. Conf. Ser.* **849**, 012028 (2017).
8. J. Deng, Y. P. Hong, S. Chen, Y. S. G. Nashed, T. Peterka, A. J. F. Levi, J. Damoulakis, S. Saha, T. Eiles, C. Jacobsen, Nanoscale x-ray imaging of circuit features without wafer etching. *Phys. Rev. B* **95**, 104111 (2017).
9. M. Holler, M. Guizar-Sicairos, E. H. R. Tsai, R. Dinapoli, E. Müller, O. Bunk, J. Raabe, G. Aeppli, High-resolution non-destructive three-dimensional imaging of integrated circuits. *Nature* **543**, 402–406 (2017).
10. M. Dierolf, A. Menzel, P. Thibault, P. Schneider, C. M. Kewish, R. Wepf, O. Bunk, F. Pfeiffer, Ptychographic X-ray computed tomography at the nanoscale. *Nature* **467**, 436–439 (2010).
11. K. Giewekemeyer, P. Thibault, S. Kalbfleisch, A. Beerlink, C. M. Kewish, M. Dierolf, F. Pfeiffer, T. Salditt, Quantitative biological imaging by ptychographic x-ray diffraction microscopy. *Proc. Natl. Acad. Sci. U.S.A.* **107**, 529–534 (2010).
12. M. Gallagher-Jones, C. S. B. Dias, A. Pryor Jr., K. Bouchmella, L. Zhao, Y. H. Lo, M. B. Cardoso, D. Shapiro, J. Rodriguez, J. Miao, Correlative cellular ptychography with functionalized nanoparticles at the Fe L-edge. *Sci. Rep.* **7**, 4757 (2017).
13. J. Deng, D. J. Vine, S. Chen, Q. Jin, Y. S. G. Nashed, T. Peterka, S. Vogt, C. Jacobsen, X-ray ptychographic and fluorescence microscopy of frozen-hydrated cells using continuous scanning. *Sci. Rep.* **7**, 445 (2017).
14. J. Deng, D. J. Vine, S. Chen, Y. S. G. Nashed, Q. Jin, N. W. Phillips, T. Peterka, R. Ross, S. Vogt, C. J. Jacobsen, Simultaneous cryo X-ray ptychographic and fluorescence microscopy of green algae. *Proc. Natl. Acad. Sci. U.S.A.* **112**, 2314–2319 (2015).
15. J. Thieme, I. McNult, S. Vogt, D. Paterson, X-ray spectromicroscopy—A tool for environmental sciences. *Environ. Sci. Technol.* **41**, 6885–6889 (2007).
16. X. Bai, G. McMullan, S. H. W. Scheres, How cryo-EM is revolutionizing structural biology. *Trends Biochem. Sci.* **40**, 49–57 (2015).
17. R. Fernandez-Leiro, S. H. W. Scheres, Unravelling biological macromolecules with cryo-electron microscopy. *Nature* **537**, 339–346 (2016).
18. J. Miao, P. Ercius, S. J. L. Billinge, Atomic electron tomography: 3D structures without crystals. *Science* **353**, aaf2157 (2016).
19. M. C. Scott, C.-C. Chen, M. Mecklenburg, C. Zhu, R. Xu, P. Ercius, U. Dahmen, B. C. Regan, J. Miao, Electron tomography at 2.4-ångström resolution. *Nature* **483**, 444–447 (2012).
20. R. Xu, C.-C. Chen, L. Wu, M. C. Scott, W. Theis, C. Ophus, M. Bartels, Y. Yang, H. Ramezani-Dakhel, M. R. Sawaya, H. Heinz, L. D. Marks, P. Ercius, J. Miao, Three-dimensional coordinates of individual atoms in materials revealed by electron tomography. *Nat. Mater.* **14**, 1099–1103 (2015).
21. Y. Yang, C.-C. Chen, M. C. Scott, C. Ophus, R. Xu, A. Pryor, L. Wu, F. Sun, W. Theis, J. Zhou, M. Eisenbach, P. R. C. Kent, R. F. Sabirianov, H. Zeng, P. Ercius, J. Miao, Deciphering chemical order/disorder and material properties at the single-atom level. *Nature* **542**, 75–79 (2017).
22. I. Robinson, R. Harder, Coherent X-ray diffraction imaging of strain at the nanoscale. *Nat. Mater.* **8**, 291–298 (2009).
23. Y. Zhao, B. W. Graf, E. J. Chaney, Z. Mahmassani, E. Antoniadou, R. De Volder, H. Kong, M. D. Boppart, S. A. Boppart, Integrated multimodal optical microscopy for structural and functional imaging of engineered and natural skin. *J. Biophotonics* **5**, 437–448 (2012).
24. S. Yue, M. N. Slipchenko, J.-X. Cheng, Multimodal nonlinear optical microscopy. *Laser Photon. Rev.* **5**, 496–512 (2011).
25. D. W. Townsend, Multimodality imaging of structure and function. *Phys. Med. Biol.* **53**, R1–R39 (2008).
26. R. Schafer, H. M. Leung, A. F. Gmitro, Multi-modality imaging of a murine mammary window chamber for breast cancer research. *BioTechniques* **57**, 45–50 (2014).
27. S. R. Cherry, Multimodality imaging: Beyond PET/CT and SPECT/CT. *Semin. Nucl. Med.* **39**, 348–353 (2009).
28. D. A. Muller, Structure and bonding at the atomic scale by scanning transmission electron microscopy. *Nat. Mater.* **8**, 263–270 (2009).
29. Y. Liu, F. Meirer, C. M. Krest, S. Webb, B. M. Weckhuysen, Relating structure and composition with accessibility of a single catalyst particle using correlative 3-dimensional micro-spectroscopy. *Nat. Commun.* **7**, 12634 (2016).
30. D. C. Hezel, P. Elangovan, S. Viehmann, L. Howard, R. L. Abel, R. Armstrong, Visualisation and quantification of CV chondrite petrography using micro-tomography. *Geochim. Cosmochim. Acta* **116**, 33–40 (2013).
31. A. W. Tait, K. R. Fisher, P. Srinivasan, J. I. Simon, Evidence for impact induced pressure gradients on the Allende CV3 parent body: Consequences for fluid and volatile transport. *Earth Planet. Sci. Lett.* **454**, 213–224 (2016).
32. R. D. Hanna, R. A. Ketcham, X-ray computed tomography of planetary materials: A primer and review of recent studies. *Geochemistry* **77**, 547–572 (2017).
33. M. R. Howells, T. Beetz, H. N. Chapman, C. Cui, J. M. Holton, C. J. Jacobsen, J. Kirz, E. Lima, S. Marchesini, H. Miao, D. Sayre, D. A. Shapiro, J. C. H. Spence, D. Starodub, An assessment of the resolution limitation due to radiation-damage in X-ray diffraction microscopy. *J. Electron Spectrosc. Relat. Phenom.* **170**, 4–12 (2009).
34. S. Marchesini, H. Krishnan, B. J. Daurer, D. A. Shapiro, T. Perciano, J. A. Sethian, F. R. N. C. Maia, SHARP: A distributed GPU-based ptychographic solver. *J. Appl. Crystallogr.* **49**, 1245–1252 (2016).
35. P. Thibault, M. Dierolf, A. Menzel, O. Bunk, C. David, F. Pfeiffer, High-resolution scanning X-ray diffraction microscopy. *Science* **321**, 379–382 (2008).
36. P. Thibault, M. Dierolf, O. Bunk, A. Menzel, F. Pfeiffer, Probe retrieval in ptychographic coherent diffractive imaging. *Ultramicroscopy* **109**, 338–343 (2009).
37. H. H. Bauschke, P. L. Combettes, D. R. Luke, Hybrid projection–reflection method for phase retrieval. *JOSA A* **20**, 1025–1034 (2003).
38. E. R. Shanblatt, C. L. Porter, D. F. Gardner, G. F. Mancini, R. M. Karl Jr., M. D. Tanksalvala, C. S. Bevis, V. H. Vartanian, H. C. Kapteyn, D. E. Adams, M. M. Murnane, Quantitative chemically specific coherent diffractive imaging of reactions at buried interfaces with few nanometer precision. *Nano Lett.* **16**, 5444–5450 (2016).
39. B. Zhang, D. F. Gardner, M. D. Seaberg, E. R. Shanblatt, H. C. Kapteyn, M. M. Murnane, D. E. Adams, High contrast 3D imaging of surfaces near the wavelength limit using tabletop EUV ptychography. *Ultramicroscopy* **158**, 98–104 (2015).
40. D. F. Gardner, M. Tanksalvala, E. R. Shanblatt, X. Zhang, B. R. Galloway, C. L. Porter, R. Karl Jr., C. Bevis, D. E. Adams, H. C. Kapteyn, M. M. Murnane, G. F. Mancini, Subwavelength coherent imaging of periodic samples using a 13.5 nm tabletop high-harmonic light source. *Nat. Photonics* **11**, 259–263 (2017).
41. A. Pryor Jr., Y. Yang, A. Rana, M. Gallagher-Jones, J. Zhou, Y. H. Lo, G. Melinte, W. Chiu, J. A. Rodriguez, J. Miao, GENFIRE: A generalized Fourier iterative reconstruction algorithm for high-resolution 3D imaging. *Sci. Rep.* **7**, 10409 (2017).
42. F. de la Peña, P. Burdet, T. Ostasevicius M. Sarahan, M. Nord, V. T. Fauske, J. Taillon, A. Eljarrat, S. Mazzucco, V. T. Fauske, G. Donval, L. F. Zagonel, I. Lyengar, M. Walls, *hyperspy: HyperSpy 0.8* (Zenodo, 2015).
43. G. Cliff, G. W. Lorimer, The quantitative analysis of thin specimens. *J. Microsc.* **103**, 203–207 (1975).
44. G. W. Lorimer, Quantitative X-ray microanalysis of thin specimens in the transmission electron microscope; a review. *Mineral. Mag.* **51**, 49–60 (1987).
45. M. Lerotic, R. Mak, S. Wirick, F. Meirer, C. Jacobsen, MANTiS: A program for the analysis of X-ray spectromicroscopy data. *J. Synchrotron Radiat.* **21**, 1206–1212 (2014).
46. J. N. Clark, C. T. Putkunz, M. A. Pfeifer, A. G. Peele, G. J. Williams, B. Chen, K. A. Nugent, C. Hall, W. Fullagar, S. Kim, I. McNulty, Use of a complex constraint in coherent diffractive imaging. *Opt. Exp. Dermatol.* **18**, 1981–1993 (2010).
47. M. W. M. Jones, A. G. Peele, G. A. van Riessen, Application of a complex constraint for biological samples in coherent diffractive imaging. *Opt. Express* **21**, 30275–30281 (2013).
48. M. W. M. Jones, K. Elgass, M. D. Junker, M. B. Luu, M. T. Ryan, A. G. Peele, G. A. van Riessen, Mapping biological composition through quantitative phase and absorption X-ray ptychography. *Sci. Rep.* **4**, 6796 (2014).
49. M. W. M. Jones, K. D. Elgass, M. D. Junker, M. D. De Jonge, G. A. Van Riessen, Molar concentration from sequential 2-D water-window X-ray ptychography and X-ray fluorescence in hydrated cells. *Sci. Rep.* **6**, 24280 (2016).
50. J. C. da Silva, P. Trtik, A. Diaz, M. Holler, M. Guizar-Sicairos, J. Raabe, O. Bunk, A. Menzel, Mass density and water content of saturated never-dried calcium silicate hydrates. *Langmuir* **31**, 3779–3783 (2015).
51. H. Yan, E. Nazaretski, K. Lauer, X. Huang, U. Wagner, C. Rau, M. Yusuf, I. Robinson, S. Kalbfleisch, L. Li, N. Bouet, J. Zhou, R. Conley, Y. S. Chu, Multimodality hard-x-ray imaging of a chromosome with nanoscale spatial resolution. *Sci. Rep.* **6**, 20112 (2016).
52. H. Yan, Y. S. Chu, J. Maser, E. Nazaretski, J. Kim, H. C. Kang, J. J. Lombardo, W. K. S. Chiu, Quantitative x-ray phase imaging at the nanoscale by multilayer Laue lenses. *Sci. Rep.* **3**, 1307 (2013).
53. B. L. Henke, E. M. Gullikson, J. C. Davis, X-ray interactions: Photoabsorption, scattering, transmission, and reflection at E = 50-30,000 eV, Z = 1-92. *At. Data Nucl. Data Tables* **54**, 181–342 (1993).
54. K. Lodders, Solar system abundances and condensation temperatures of the elements. *Astrophys. J.* **591**, 1220–1247 (2003).
55. A. J. Brearley, Origin of graphitic carbon and pentlandite in matrix olivines in the allende meteorite. *Science* **285**, 1380–1382 (1999).
56. J. C. Sánchez-López, A. Caballero, A. Fernández, Characterisation of passivated aluminium nanopowders: An XPS and TEM/EELS study. *J. Eur. Ceram. Soc.* **18**, 1195–1200 (1998).
57. Y. K. Chang, K. P. Lin, W. F. Pong, M.-H. Tsai, H. H. Hseih, J. Y. Pieh, P. K. Tseng, J. F. Lee, L. S. Hsu, Charge transfer and hybridization effects in Ni3Al and Ni3Ga studies by x-ray-absorption spectroscopy and theoretical calculations. *J. Appl. Phys.* **87**, 1312–1317 (2000).
58. B. He, M. Zhou, Z. Hou, G. Li, Y. Kuang, Facile synthesis of Ni3S2/rGO nanosheets composite on nickel foam as efficient electrocatalyst for hydrogen evolution reaction in alkaline media. *J. Mater. Res.* **33**, 519–527 (2018).
59. T. Yoshimura, Y. Tamenori, N. Iwasaki, H. Hasegawa, A. Suzuki, H. Kawahata, Magnesium *K*-edge XANES spectroscopy of geological standards. *J. Synchrotron Radiat.* **20**, 734–740 (2013).

60. A. J. Westphal, A. L. Butterworth, J. A. Tomsick, Z. Gainsforth, Measurement of the oxidation state of Fe in the ISM using X-ray absorption spectroscopy. *Astrophys. J.* **872**, 66 (2019).
61. F. Bourdelle, K. Benzerara, O. Beyssac, J. Cosmidis, D. R. Neuville, G. E. Brown Jr., E. Paineau, Quantification of the ferric/ferrous iron ratio in silicates by scanning transmission X-ray microscopy at the Fe $L_{2,3}$ edges. *Contrib. Mineral. Petrol.* **166**, 423–434 (2013).
62. M. Miyahara, A. El Goresy, E. Ohtani, M. Kimura, S. Ozawa, T. Nagase, M. Nishijima, Fractional crystallization of olivine melt inclusion in shock-induced chondritic melt vein. *Phys. Earth Planet. Inter.* **177**, 116–121 (2009).
63. L. Bonal, E. Quirico, M. Bourot-Denise, G. Montagnac, Determination of the petrologic type of CV3 chondrites by Raman spectroscopy of included organic matter. *Geochim. Cosmochim. Acta* **70**, 1849–1863 (2006).
64. C. T. Chantler, Theoretical form factor, attenuation, and scattering tabulation for *Z*=1–92 from *E*=1–10 eV to *E*=0.4–1.0 MeV. *J. Phys. Chem. Ref. Data.* **24**, 71–643 (1995).
65. C. T. Chantler, Detailed tabulation of atomic form factors, photoelectric absorption and scattering cross section, and mass attenuation coefficients in the vicinity of absorption edges in the soft x-ray (*Z*=30–36, *Z*=60–89, *E*=0.1 keV–10 keV), addressing convergence issues of earlier work. *J. Phys. Chem. Ref. Data* **29**, 597–1048 (2000).
66. R. W. Shewman, L. A. Clark, Pentlandite phase relations in the Fe–Ni–S system and notes on the monosulfide solid solution. *Can. J. Earth Sci.* **7**, 67–85 (1970).
67. V. Raghavan, Fe-Ni-S (iron-nickel-sulfur). *J. Phase Equilib. Diffus.* **25**, 373–381 (2004).
68. C.-T. Liao, Y. H. Lo, J. Zhou, A. Rana, C. S. Bevis, G. Gui, B. Enders, K. Cannon, D. Shapiro, C. Bennett, H. Kapteyn, R. Falcone, J. Miao, M. Murnane, SQUARREL: Scattering quotient analysis to retrieve the ratio of elements in x-ray ptychography. *Microsc. Microanal.* **25**, 112–113 (2019).
69. M. Chen, T. G. Sharp, A. El Goresy, B. Wopenka, X. Xie, The majorite-pyrope + magnesiowüstite assemblage: Constraints on the history of shock veins in chondrites. *Science* **271**, 1570–1573 (1996).
70. T. G. Sharp, P. S. de Carli, Shock effects in meteorites, in *Meteorites and the Early Solar System II* (University of Arizona Press, 2006), pp. 653–677.
71. D. Stöffler, K. Keil, E. R. D. Scott, Shock metamorphism of ordinary chondrites. *Geochim. Cosmochim. Acta* **55**, 3845–3867 (1991).
72. J. I. Goldstein, E. R. D. Scott, N. L. Chabot, Iron meteorites: Crystallization, thermal history, parent bodies, and origin. *Geochemistry* **69**, 293–325 (2009).
73. U. B. Marvin, J. A. Wood, J. S. Dickey Jr., Ca-Al rich phases in the allende meteorite. *Earth Planet. Sci. Lett.* **7**, 346–350 (1970).
74. L. Grossman, Petrography and mineral chemistry of Ca-rich inclusions in the Allende meteorite. *Geochim. Cosmochim. Acta* **39**, 433–434 (1975).
75. F. J. Ciesla, Outward transport of high-temperature materials around the midplane of the solar nebula. *Science* **318**, 613–615 (2007).
76. ALS Upgrade, ALS-U overview; https://als.lbl.gov/als-u/overview/.

Acknowledgments

Funding: J.M., H.K., and M.M. acknowledge support for this work by STROBE: A National Science Foundation Science & Technology Center, under grant no. DMR 1548924. J.M. acknowledges partial support of the Department of Energy (DE-SC0010378) for the development of GENFIRE. C.S.B. acknowledges support from the NSF GRFP. We acknowledge the support of NVIDIA Corporation for the donation of the Quadro K5200 GPU used for this research. C.B. and K.M.C. acknowledge support from NASA, SSERVI (Solar System Exploration Research Virtual Institute), and CLASS (Center for Lunar and Asteroid Surface Science) under grant no. NNA14AB05A. X-ray imaging performed at COSMIC used resources of the Advanced Light Source, which is a DOE Office of Science User Facility under contract no. DE-AC02-05CH11231. HAADF-STEM imaging and EDS mapping with TitanX were performed at the Molecular Foundry, which is supported by the Office of Science, Office of Basic Energy Sciences of the U.S. DOE under Contract No. DE-AC02-05CH11231. **Author contributions:** J.M. directed the project. Y.H.L., J.M., C.B., D.S., M.M., H.K., and R.F. planned the experiments. D.S., K.M.C., and C.B. provided the samples. J.Z. collected the HAADF and EDS data. Y.H.L., A.R., C.-T.L., C.S.B., G.G., B.E., D.S., R.F., and J.M. collected the ptychography and STXM data. C.S.B. performed the reconstructions of ptychographic images. Y.H.L. performed the tomography reconstructions. A.R., Y.H.L., and C.-T.L. conducted the data analysis. C.-T.L. developed SQUARREL with inputs from Y.H.L. and other authors. Y.-S.Y., R.C., and K.N. built the COSMIC beamline. All authors contributed to the discussion and writing of the manuscript. **Competing interests:** H.K. is the Chief Technology Officer of Kapteyn-Murnane Laboratories Inc., which is working on similar short-wavelength imaging techniques. The authors declare no other competing interests. **Data and materials availability:** All data needed to evaluate the conclusions in the paper are present in the paper and/or the Supplementary Materials. Ptychography data presented in this work are available for download at CXIDB (ID 102), and STXM spectromicroscopy, HAADF-STEM, and EDS tomography data presented in this work are available for download at Mendeley Data (doi:10.17632/8275525mh8.1). Additional data related to this paper may be requested from the authors.

Submitted 15 March 2019
Accepted 23 August 2019
Published 20 September 2019
10.1126/sciadv.aax3009

Citation: Y. H. Lo, C.-T. Liao, J. Zhou, A. Rana, C. S. Bevis, G. Gui, B. Enders, K. M. Cannon, Y.-S. Yu, R. Celestre, K. Nowrouzi, D. Shapiro, H. Kapteyn, R. Falcone, C. Bennett, M. Murnane, J. Miao, Multimodal x-ray and electron microscopy of the Allende meteorite. *Sci. Adv.* **5**, eaax3009 (2019).